Article

Surface Subsidence Monitoring Induced by Underground Coal Mining by Combining DInSAR and UAV Photogrammetry

Yafei Zhang [1], Xugang Lian [1,*], Linlin Ge [1,2], Xiaoyu Liu [1], Zheyuan Du [2,3], Wenfu Yang [4,5], Yanru Wu [1], Haifeng Hu [1] and Yinfei Cai [1]

[1] School of Mining Engineering, Taiyuan University of Technology, Taiyuan 030024, China
[2] School of Civil and Environmental Engineering, UNSW Australia, Sydney, NSW 2052, Australia
[3] Positioning and Community Safety Division, Geoscience Australia, Canberra, ACT 2061, Australia
[4] Shanxi Provincial Key Laboratory of Resources, Environment and Disaster Monitoring, Shanxi Coal Geology Geophysical Surveying Exploration Institute, Jinzhong 030600, China
[5] Key Laboratory of Monitoring and Protection of Natural Resources in Mining Cities, Ministry of Natural Resources, Jinzhong 030600, China
* Correspondence: lianxugang@tyut.edu.cn

Abstract: Surface subsidence caused by coal mining has become an important factor that affects and restricts the sustainable development of mining districts. It is necessary to use appropriate methods for effective subsidence monitoring. It is hard to monitor large gradient ground deformations with a high accuracy by using differential interferometric synthetic aperture radar (DInSAR) technology. Unmanned aerial vehicle (UAV) photogrammetry is limited in that it monitors the basin edge by subtracting two DEMs (digital elevation models). Therefore, in this paper we propose a combination of DInSAR and UAV photogrammetry to complement the two data advantages and to achieve a high-precision monitoring of mining subsidence areas. The subsidence of coal panel 81,403 in the Yangquan coal mine was obtained using DInSAR and UAV photogrammetry technologies. The appropriate fusion points were selected for the two datasets and the agreement between the fusion data and the leveling data was verified. The results indicated that the combination of DInSAR and UAV technology could monitor the settlement more accurately than the single use of DInSAR or UAV technology.

Keywords: subsidence monitoring; DInSAR; UAV photogrammetry; fusion data; leveling

1. Introduction

Coal is one of the important energy sources in the world and coal mining in several countries is an important and basic industry for the national economy. Whilst coal resources bring a great economic benefit, their over-exploitation causes surface subsidence and environmental disasters. This brings significant ecological and environmental risks to mining areas and threatens the safety of lives and property in mining areas [1]. A ground subsidence basin is gradually formed in the process of the working face advancing. Therefore, it is necessary to find ways to achieve the effective monitoring of the surface in coal mining areas to determine the movement rules and minimize the associated mining losses. This significantly influences disaster assessment, comprehensive management, and planning in mining areas [2,3]. Traditional mining area deformation monitoring methods such as leveling and global navigation satellite systems (GNSSs) have previously been widely used for deformation monitoring in mining areas. However, with the development of production demands, traditional monitoring methods have a difficulty in achieving large-scale and long-term dynamic monitoring because of shortcomings such as their large working intensity, long operational cycle, significant weather impact, small monitoring scope, and deformation monitoring points buried on the surface being prone to damage [4,5].

In this era of the fast development of remote sensing technologies, space-borne synthetic aperture radar (SAR), visible spectrum remote sensing, unmanned aerial vehicles (UAVs), and other technologies have been applied to deformation monitoring to varying degrees. As a new earth observation technology, differential interferometric SAR (DInSAR) has the advantages of a wide coverage, a high resolution, high accuracy, all-weather, all-day operations, and a low cost. It is sensitive to the small deformation monitoring of surfaces and can effectively obtain such information in mining areas. The observation accuracy can reach the centimeter or even millimeter level [6–9]. This approach has been widely used in ground subsidence monitoring induced by underground coal mining. Gabriel et al. [10] demonstrated the initial use of DInSAR technology to detect ground deformation at the cm level, opening a new chapter in the monitoring of surface deformation with InSAR technology. Carnec et al. [11] used three ERS-1 images, showing for the first time that DInSAR technology could be used to monitor subsidence in mining areas. Since then, researchers have conducted further studies on how to accurately obtain deformation using DInSAR or time series InSAR technology [12–15]. In the process of InSAR data processing, Ge et al. [16] used GPS measurements as ground control points to reduce the error of the InSAR results and achieve the high-precision monitoring of subsidence caused by underground mining. Lian et al. [17] fused Sentinel-1A and Sentinel-1B data to realize the high-precision monitoring of subsidence in the Datong mining area of China. The proposed method improved the time resolution of the DInSAR technologies.

UAVs also have advantages of flexibility, being fast and efficient, a low cost, high spatial and temporal accuracies for image acquisition, and all-weather monitoring. With the continuous advent of various high-precision, light and small sensors, UAV photogrammetry technology has been applied in various degrees in geographical mapping, land and resources surveys, disaster prevention, and other fields. Compared with traditional monitoring methods, the information obtained by UAVs is more visible and richer and has good application prospects for deformation monitoring [18–20]. Chen et al. [21] collected topographic information as a digital surface model (DSM) in open-pit mines using a UAV. Ge et al. [22] studied the application of UAVs in the Ulan and Tahmoor mines, respectively. It preliminarily confirmed the feasibility of UAVs in monitoring side slope stability and underground subsidence. Wikaa et al. [23] successfully monitored the discontinuous deformation of a mining area by using UAV photogrammetry technology. Lian et al. [24] realized surface subsidence monitoring at the Yangquan coal mine area in China using UAV photogrammetry. These results show that UAV technologies have high monitoring accuracies in large gradient deformation areas. However, the accuracy of small deformation areas at the edge of subsidence basins requires further improvement.

DInSAR technology is affected by many factors, including the orbit error and atmospheric delay [25]. A local surface deformation gradient that is too large will weaken the quality of the interference phase and cause decoherence in the interference image pairs, which significantly reduces the accuracy of DInSAR monitoring [26–29]. The accuracy of coal mining subsidence data from UAVs is less than the millimeter level, making it difficult to monitor small subsidence deformations at the edge of mining areas and providing a poor edge deformation expression ability [24]. The ground movement and deformation induced by mining is a complex time and space process. Both the single DInSAR or UAV technologies have difficulty in obtaining the complete subsidence basin information of mining areas. Zhang et al. [30] monitored the deformation of the Tianziling landfill from millimeter to millimeter using InSAR and UAV technologies. The results showed that these two technologies have a mutual verification in landfill monitoring. Deffontaines et al. [31] determined the structural geometry of the Pingting terraces through the method of obtaining a digital terrain model (DTM) by using UAV technology and then used InSAR time series interferometry to analyze the interseismic deformation. Meng et al. [32] combined InSAR with UAV photogrammetry technology to study the loess landslide of Hongheyan in Northwest China. It was found that InSAR has greater advantages in monitoring creeping deformation and UAV technology was more suitable for monitoring large sudden slides.

At present, there are few studies on the joint monitoring of mining subsidence by using InSAR and UAV technologies. In this paper, we propose a method to combine them to monitor surface subsidence deformation in mining areas. This approach complements the advantages of the two technologies to comprehensively monitor and analyze the surface subsidence of mining areas.

2. Study Area and Datasets

2.1. Study Area

From the Yangquan coal mine, Shanxi Province, China, coal panel 81,403 was selected as the study area. The strike length of the panel was 1345 m, the dip length of the panel was 226 m, the average mining depth was 446.8 m, the average dip angle of the coal seam was 4°, and the average coal thickness of the working face was 7.24 m. The working face began to be mined in October 2019. The topography of the mining area was high in the middle and low in the north and south. There was low vegetation on the surface of the working face, but the ground was not completely covered. Three observation lines were arranged above the surface: a half-strike observation line was arranged, which was line A, and two dip observation lines were arranged; namely, line B and line C. The ground subsidence of line A and line C was analyzed in this study. Line A contained 33 effective monitoring points and line C contained 17 effective monitoring points. The position of the study area, working face, and measured leveling point is shown in Figure 1. In Figure 1, AK1 and AK2 are the control points of observation line A; BK1, BK2, and BK3 are the control points of observation line B; and CK1 and CK2 are the control points of observation line C. The black framework in Figure 1 is the working face boundary. The geological profile of the study area is shown in Figure 2. The coal-bearing strata in the mining area were mainly the Taiyuan Formation and Shanxi Formation, containing 6–15 coal seams. The minable coal seams in the minefield were 3#, 6#, 8#, 12#, and 15#.
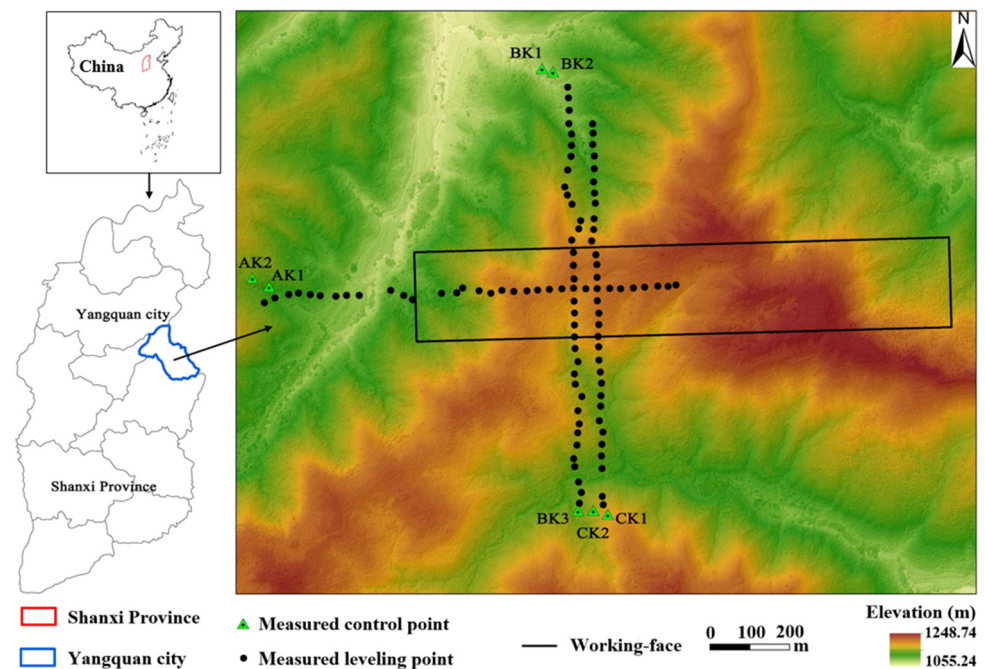
Figure 1. The geographic position of study area, working face, and measured leveling point.
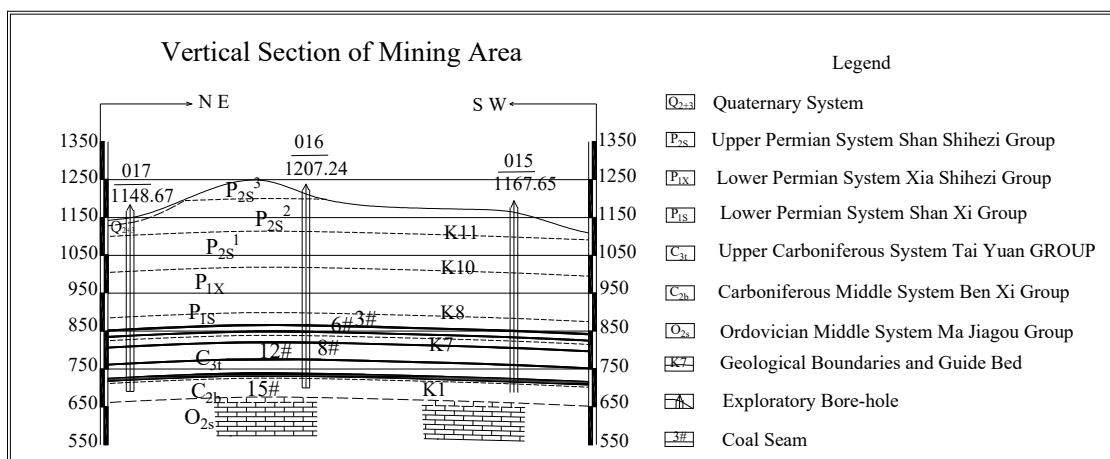
Figure 2. Vertical section of mining area. # represents coal seam number.

2.2. Datasets

The image data from Sentinel-1A, launched by ESA in 2014, were used. ESA headquarters in Paris, France. Single look complex (SLC) images with the interference width (IW) mode were selected with a spatial resolution of 5 m × 20 m. Four ascending images covering the study area obtained from 14 June, 26 June, 8 July, and 20 July 2020 were processed. The external DEM was shuttle radar topography mission (SRTM) data; data with a 30 m resolution were selected. The parameters of the interference data are shown in Table 1.

Table 1. Data information of Sentinel-1A for the study area.

Interference Image Pairs	Acquisition Date		Time-Baseline (d)	Datatype
	Main Image	Secondary Image		
1	14 June 2020	26 June 2020	12	
2	26 June 2020	8 July 2020	12	IW (SLC)
3	8 July 2020	20 July 2020	12	

The UAV data collection for the study area was conducted on 14 June and 20 July 2020, respectively. The UAV flight platform used was the D2000 FEIMA Intelligent Aerial Survey System, equipped with a visible light D-CAM2000 sensor. The system was a multi-rotor UAV system with a small size, long endurance, and high-precision mapping application. The equipment was stored in a special box, which was compact, portable, and convenient for field work. The route plan and parameter setting were performed using the UAV manager software. The parameters were set according to the actual condition of the study area to ensure both data quality and flight safety. The forward overlap was set to 80% and the side overlap was set to 70%. The ground resolution was designed to be 4 cm. The drone automatically took off after confirming the flight safety.

The coordinates for and height information of each monitoring point were obtained by adjustments and inspections using total station and GPS measurement methods; thus, the leveling data were finally obtained. The leveling data acquisition time in the study area was 14 June and 21 July 2020, which did not fully match with the acquisition time of the SAR images and UAV data. It was necessary to interpolate the leveling data according to the time interval to obtain the leveling data on 20 July 2020. The two periods of data were then subtracted to obtain the surface subsidence obtained by the leveling method.

3. Research Methods

3.1. DInSAR Data Processing

Combined with the external DEM, SARscape software was used to process the image pairs discussed in Table 1. The software was developed by the Swiss SARmap company based on an ENVI remote sensing image processing platform. The software version used for this data processing is ENVI5.3. A two-pass approach was used in the processing. The main processing included the image registration, interferogram generation, adaptive filtering, coherent generation, phase unwrapping, geocoding, and phase rotation deformation. To reduce the influence of the time baseline on the image coherence, the data were divided into three interference image pairs based on the time series in the processing to ensure the minimum time interval for each interference image pair. The one-dimensional deformation of the radar line of sight (LOS) was obtained by DInSAR; the LOS deformation was then converted into the vertical deformation to obtain the settlement result. Finally, ArcGIS was used to superimpose the difference results and obtain the difference from 14 June to 20 July 2020 (Figure 3). The DInSAR monitoring values for each monitoring point were extracted and compared with the leveling data. The comparison results of the two are shown in Figure 4. The "Measured subsidence" in Figure 4 denotes the leveling data. And Line A, Line B and Line C are marked with letters A, B and C respectively.
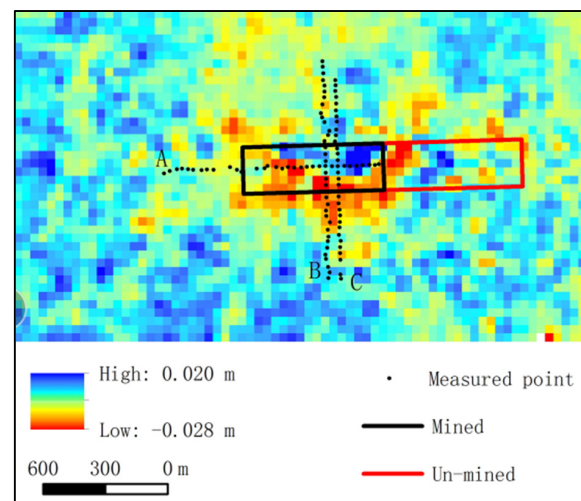
Figure 3. Illustration of the DInSAR processing results.
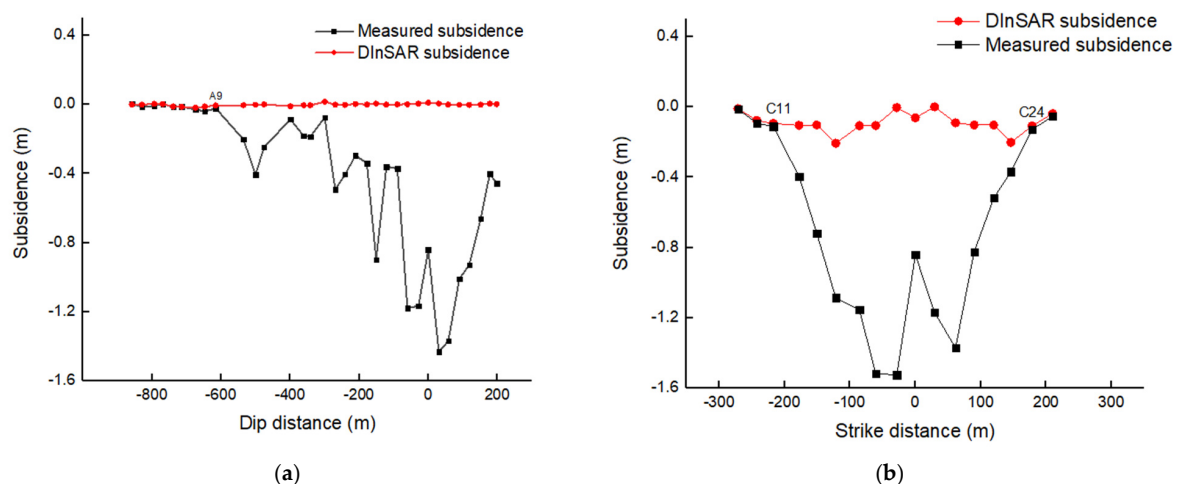
Figure 4. Comparison between the DInSAR monitoring and leveling data along line A (**a**) and line C (**b**).

The experimental results showed that the DInSAR monitoring before the ninth monitoring point along line A (A9) was consistent with the leveling data. After the A9 monitoring point, a large subsidence magnitude caused decoherence in the DInSAR and provided incorrect monitoring results. The actual subsidence increased near the center of the subsidence basin, but the value—as monitored by DInSAR in this region—was still relatively small. Thus, the entire ground subsidence basin information could not be extracted. The same result was true for line C. Figure 3 reveals that there was an obvious decoherence in the center area of the subsidence basin. Thus, the DInSAR monitoring value was quite different from the leveling data. We concluded that large settlements greatly influenced the DInSAR monitoring results. The points with small settlements at the edge had small errors and the points with large settlements at the center had large errors. In the large subsidence area, the correct subsidence value could not be effectively monitored, which is part of the characteristics of DInSAR monitoring for small deformations.

3.2. UAV Data Processing

In this study, we processed the original data using UAV manager software. The dense matching point cloud, DSM, and digital orthophoto map (DOM) were obtained based on the structure from motion (SFM). Point cloud filtering was performed using the automated filtering tool in Terrascan software, which was developed by Terrasolid company, Finland. The filtered ground points were then obtained by an inverse distance weighted interpolation method to acquire the DEM data for 14 June and 20 July 2020. The DEM on 14 June was then subtracted from the DEM on 20 July to obtain the surface subsidence basin in the study area between these times (Figure 5). In Figure 5: Line A, Line B and Line C are marked with letters A, B and C respectively. The red framework is the working face boundary, and the blue framework is the mined boundary. The UAV monitoring values for each point were extracted and compared with the measured leveling data in Figure 6.
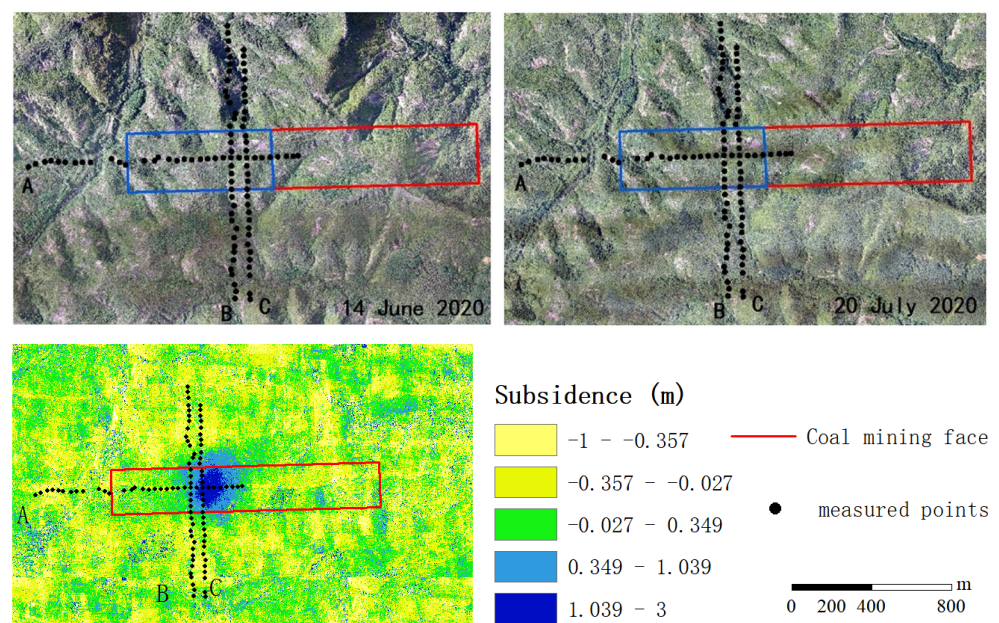
Figure 5. Subtraction of DEM maps from two different times as taken from a UAV.
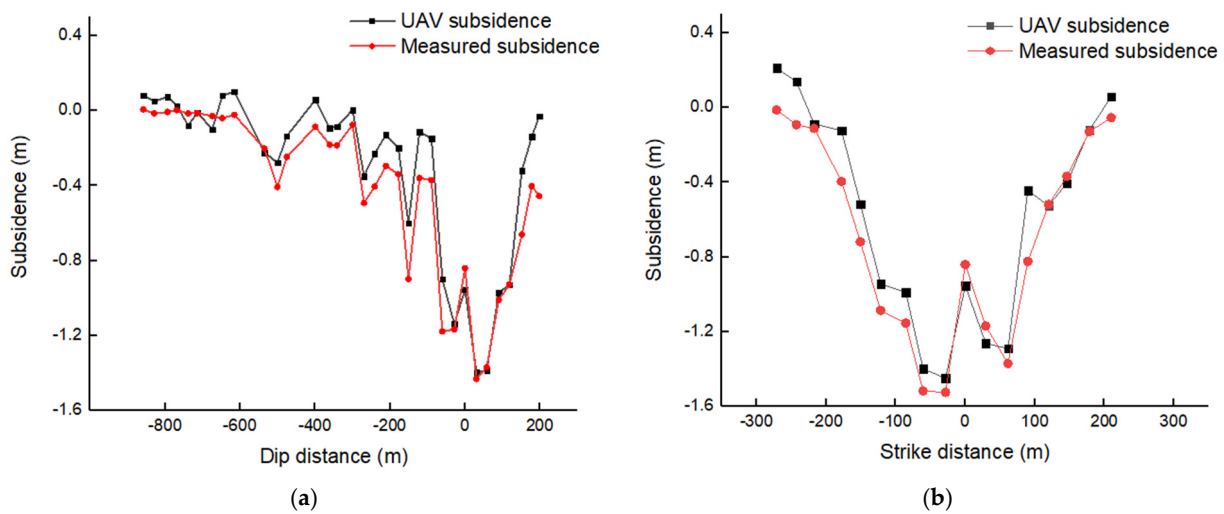
Figure 6. Comparison of UAV monitoring and leveling data along line A (**a**) and line C (**b**).

Large subsidence can be monitored by UAV technology; it is formed in the process of advancing the working face and the surface above the working face is affected by mining. By comparing the subsidence obtained by the UAV with the leveling data, we found that the error was small near the maximum subsidence value and the error was large at the edge of the basin with the small subsidence. In summary, the UAV photogrammetry technology could monitor the maximum subsidence and reflect the overall subsidence trend, but it was not sensitive to a small deformation.

3.3. Data Fusion of DInSAR and UAV

Points with a subsidence value of 10 mm are generally used as boundary points for surface subsidence basins [33]. However, the observation accuracy of DInSAR technology can reach the millimeter level. As shown in Figure 7, under the influence of mining, a subsidence basin larger than the mined-out area is formed on the surface. The numbers in Figure 7 represent different points on the ground, and it can be seen that the movement direction of each point in the basin points to the center of the basin. The subsidence value at the edge of the basin is small; therefore, in order to monitor and analyze the ground subsidence more completely and accurately, DInSAR technology was used to monitor the edge of the ground subsidence basin with a small deformation and UAV technology was used to monitor the center of the ground subsidence basin with a large gradient deformation.
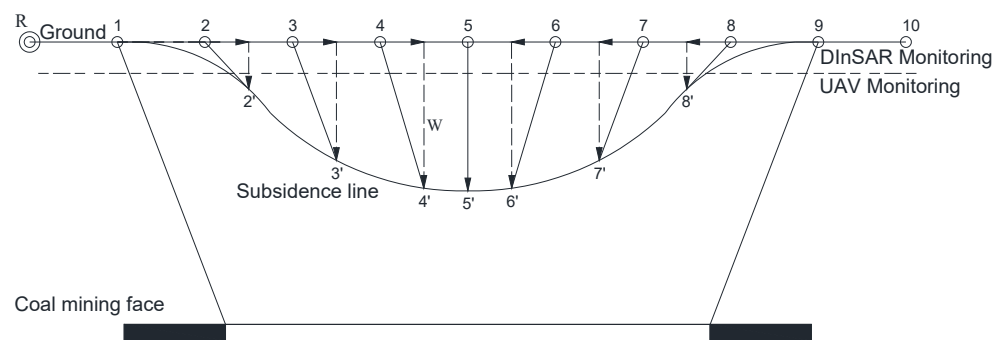
Figure 7. Surface movement basin graph.

3.3.1. Threshold Value of DInSAR Results

The coherence coefficient of the DInSAR interference was used to screen the DInSAR monitoring values. Baran et al. [34] considered the influence of the coherence coefficient on the detectable deformation gradient of DInSAR and obtained the following mathematical model:

$$D_{\max} = d_{\max} + 0.002(\gamma - 1) \tag{1}$$

where $D_{\max}$ indicates the ability of the InSAR to monitor the maximum deformation gradient, γ is the coherence coefficient after interference ranging from 0 to 1, and $d_{\max}$ is the maximum theoretical deformation gradient that can be detected by DInSAR. It can be seen from this formula that as the coherence increases, the $D_{\max}$ increases accordingly. When $\gamma = 1$, $D_{\max} = d_{\max}$ and the maximum detectable deformation gradient is equal to the maximum theoretical deformation gradient that can be detected by DInSAR. Various decorrelation factors such as atmospheric delay and the natural attenuation of scatterers cause a SAR image loss correlation, making the detectable deformation gradient of DInSAR generally far less than its theoretical value.

For C-band Sentinel-1A images with a 20 m resolution, the maximum detectable deformation gradient of the DInSAR is nearly 0 when the coherence coefficient is less than 0.3. Therefore, this value was used as the screening threshold for DInSAR monitoring. The coherence coefficient of each monitoring point was extracted; the coherence coefficient of the A12 monitoring point after A9 was less than 0.3. Points closer to the center of the subsidence basin gave lower coherence coefficients and even exhibited a decoherence phenomenon. Therefore, DInSAR monitoring was used for the A9 monitoring points and before (near the basin edge). For line C, the coherence coefficient of the monitoring points between C11 and C24 was less than 0.3. Therefore, DInSAR monitoring was used for the C11 monitoring point and before, and at C24 and after.

3.3.2. Threshold Value of UAV Results

The UAV monitoring results for each monitoring point were extracted and the threshold T for the UAV monitoring was obtained based on the formula:

$$T = \pm\sqrt{\frac{\sum\limits_{i=1}^{n}(U_i - W_i)^2}{n}} \tag{2}$$

where U_i is the UAV monitoring value of the ith monitoring point, W_i is the measured leveling value of the ith monitoring point, and n is the number of monitoring points. This threshold was used to screen the monitoring values obtained from the UAV. Points where the UAV monitoring value was greater than the threshold, which were the furthest away from the center of the subsidence basin, were selected.

The calculated threshold for the UAV monitoring of line A was 0.162 m. Compared with the UAV monitoring values at each monitoring point, the value of the A9 monitoring point was 0.104 m, which was less than the threshold of 0.162 m. In the A12 monitoring point (after A9), the UAV monitoring value was 0.224 m, which was greater than the threshold. Therefore, the DInSAR monitoring value was used before the A9 monitoring point and the UAV was used after that. This brought the fused monitoring value closer to the measured data. For line C, the threshold for the UAV monitoring was 0.171 m. Comparing the UAV monitoring values at each monitoring point suggested that only the UAV monitoring value of monitoring point C11 was greater than the threshold. Considering the superiority of DInSAR at monitoring the basin edge, the monitoring points between C11 and C24 were taken from the UAV and the rest were from DInSAR.

As seen from Figure 8, the differences between the DInSAR and UAV monitoring values before the A9 monitoring point were not significant. After A9, the deformation gradient of the subsidence basin increased and the difference between the DInSAR and UAV monitoring values suddenly increased. When approaching the center of the basin, a

significant difference appeared between the UAV and DInSAR monitoring values, indicating that the DInSAR was uncertain in the area behind the A9 monitoring point as it had exceeded its monitoring range and had inaccurate results. Therefore, the A9 monitoring point was selected as the fusion point; DInSAR was used on and before this point and the UAV was used after.
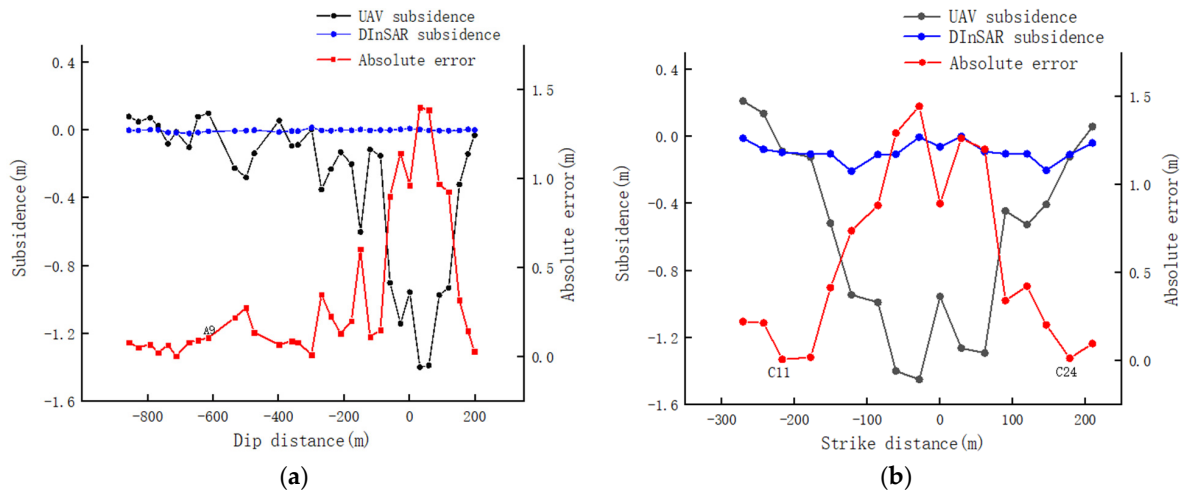
Figure 8. Comparison of DInSAR and UAV monitoring values along line A (**a**) and line C (**b**).

Figure 8 also shows that as the deformation gradient of the subsidence basin increased between the C11 and C24 monitoring points, the UAV and DInSAR significantly differed. This indicated that there was uncertainty in the DInSAR between these points as it exceeded the monitoring range of the DInSAR and resulted in inaccurate monitoring results.

3.3.3. Null Value Processing after Fusion

If there are nulls in the monitoring points between the fused data, the inverse distance weighting method can be used to determine the monitoring values of these intermediate points. That is, from the distance $d_j = \sqrt{(m_i - m_j)^2 + (n_i - n_j)^2}$ between the monitoring points (m_i, n_i) and (m_j, n_j), the null value is calculated as:

$$W_i = \sum_{j=1}^{n} \frac{d_j}{\sum\limits_{j=1}^{n} d_j} W_j \tag{3}$$

where i is the point to be solved, j is the monitoring point around the point to be solved, and W_i and W_j represent the monitoring values of the corresponding points. As there was no value between the fusion boundaries of the DInSAR and UAV monitoring points on lines A and C in this experiment, no inverse distance weighting was required to calculate the null values.

3.3.4. Coherence Test

To ensure the fused data could accurately express the settlement of the working face, we needed to verify the calculation results. The fusion and leveling data were regarded as two samples. The correlation coefficient of the samples was used to analyze the relationship between the two groups of data, which was shown as:

$$\rho = \frac{\sum\limits_{i=1}^{n} (x_i - \overline{x})(y_i - \overline{y})}{\sqrt{\sum\limits_{i=1}^{n} (x_i - \overline{x})^2} \sqrt{\sum\limits_{i=1}^{n} (y_i - \overline{y})^2}} \tag{4}$$

where, ρ represents the correlation coefficient between the leveling data (x_i) and fusion data (y_i), $\overline{x}$ represents the means of the leveling data, and $\overline{y}$ represents the means of the fusion data. For line A, the correlation coefficient between the two datasets was 0.960. For a significance factor of $\alpha = 0.01$, there were 31 ($n-2$) degrees of freedom and the corresponding correlation coefficient threshold was 0.442. For line C, the correlation coefficient between the two datasets was 0.971. For a significance factor of $\alpha = 0.01$, there were 17($n-2$) degrees of freedom and the corresponding correlation coefficient threshold was 0.575. As a comparison, both lines A and C showed a high correlation between the leveling and fusion data. The fusion results for lines A and C are shown in Figures 9 and 10, respectively.
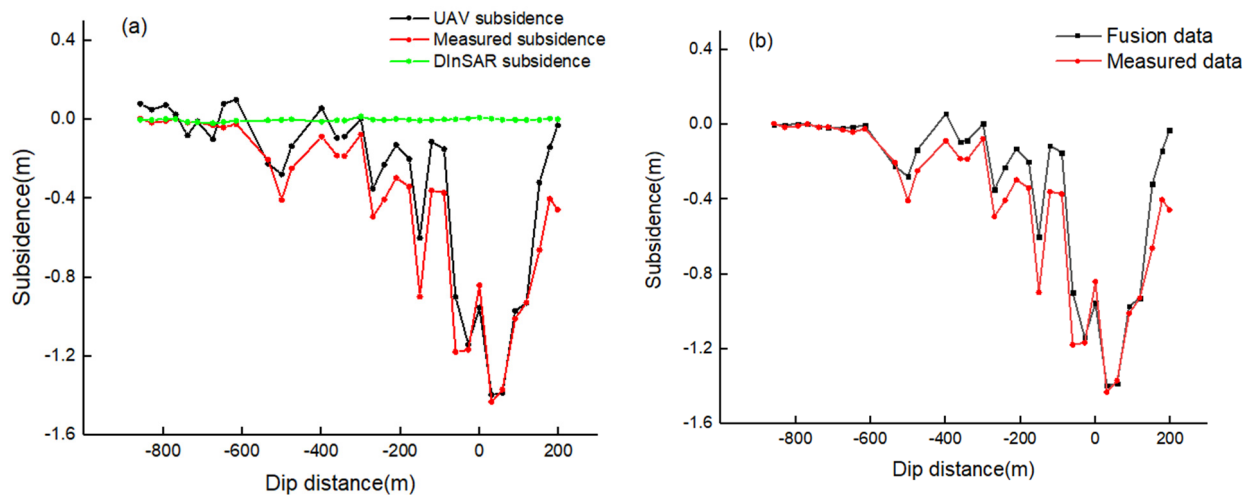
Figure 9. Results before fusion (**a**) and after fusion (**b**) along line A.
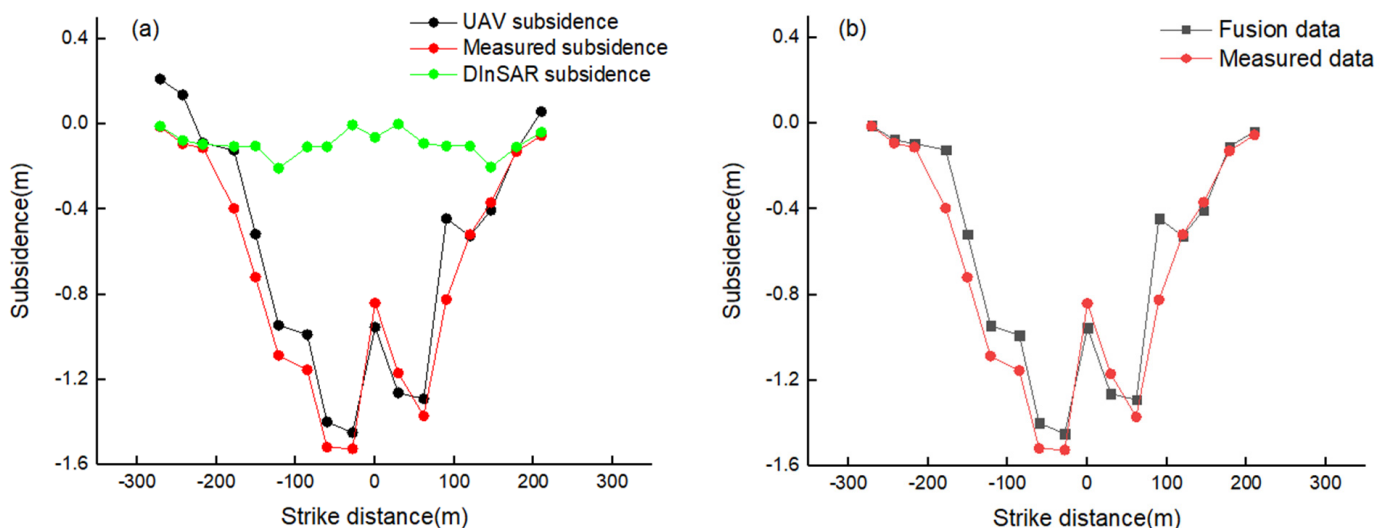
Figure 10. Results before fusion (**a**) and after fusion (**b**) along line C.

4. Experimental Results and Analysis

Based on the leveling data of the study area, the maximum absolute error, mean absolute error (MAE), and root mean square error (RMSE) were calculated to verify the accuracy of the method of combining DInSAR and UAV technologies. Table 2 indicates that before the fusion boundary of the A9 monitoring point, the monitoring accuracy of the DInSAR was higher than that of the UAV, which also reflected the superiority of the DInSAR technology in monitoring the edges of the subsidence basins. The UAV had poor edge expression abilities, making it difficult to monitor small subsidence deformations. Near the center of basin after the A9 measuring point, the accuracy of the DInSAR was

far less than that of the UAV. This was because the DInSAR exhibited incoherence when monitoring a large gradient subsidence, which resulted in inaccurate monitoring. The UAV could accurately monitor large gradient surface subsidence with its advantage of monitoring large deformations. This also explained the results for line C; the combination of the DInSAR and UAV monitoring methods could improve the accuracy of deformation monitoring in mining areas (Table 3).

Table 2. Accuracy comparison between the single means and fusion monitoring along line A.

Monitoring Method	Maximum Absolute Error (m)		MAE (m)		RMSE (m)	
	Outside Fusion Border	Within Fusion Border	Outside Fusion Border	Within Fusion Border	Outside Fusion Border	Within Fusion Border
DInSAR	0.043	1.427	0.022	0.579	0.025	0.706
UAV	0.123	0.426	0.070	0.150	0.079	0.186
Fusion monitoring	0.426		0.112		0.159	

Table 3. Accuracy comparison between the single means and fusion monitoring along line C.

Monitoring Method	Maximum Absolute Error (m)		MAE (m)		RMSE (m)	
	Outside Fusion Border	Within Fusion Border	Outside Fusion Border	Within Fusion Border	Outside Fusion Border	Within Fusion Border
DInSAR	0.016	1.521	0.018	0.859	0.018	0.995
UAV	0.273	0.166	0.188	0.118	0.211	0.160
Fusion monitoring	0.272		0.103		0.145	

The fused subsidence line reflected that the farther away from the center of the mining area, the smaller the subsidence value; the closer to the center of the mining area, the larger the subsidence value. The shape of the subsidence line conformed with the general law of mining subsidence.

5. Discussion

(1) Through the difference processing of the Sentinel-1A data, the subsidence of the monitoring points on the working face of the study area was extracted and compared with the measured leveling data. The comparative results revealed that the image was incoherent due to settlement and mutation, which significantly influenced the DInSAR monitoring results. The points with small settlements had small errors. For points with large settlements in the center of the subsidence basin, the settlement—as obtained by DInSAR—was still relatively small; thus, the correct settlement value could not be effectively monitored. This agreed with the characteristics of the DInSAR monitoring of regions with small deformations.

(2) The monitoring value obtained via UAV photogrammetry was compared with the measured leveling data. The results indicated that the maximum subsidence could be monitored using UAVs, which comprehensively reflected the influence range of the mining subsidence. However, it was difficult to monitor the edges of the mining areas with a high precision, giving a poor edge expression ability. Therefore, the UAV technologies could not effectively monitor small subsidence deformations.

(3) Monitoring mining subsidence could be realized through the combination of DInSAR and UAV technologies. The monitoring values for the DInSAR and UAV were screened, an appropriate point was found to fuse the two datasets, and a coherence test was performed to verify the fusion results, which suggested that the fused data were highly correlated with the measured level data. The RMSE of the subsidence values for observation line A after fusion was 0.159 m. The RMSE of the subsidence values for

observation line C after fusion was 0.145 m. The accuracy of the results improved compared with the results of the DInSAR or UAV, which proved that the determined fusion threshold values were reasonable. However, as DInSAR technologies can only obtain one-dimensional deformations in the radar line of sight (LOS), and this study only realized the monitoring of one-dimensional subsidence of the target area, realizing the high-precision monitoring of the three-dimensional (3D) deformation of mining districts by combining InSAR and UAV technologies is worthy of a future study.

6. Conclusions

DInSAR and UAV technologies were combined to monitor the ground subsidence of the working face of coal panel 81,403 in Yangquan Coal Mine. The following conclusions were obtained:

(1) The high-precision monitoring ability of DInSAR was primarily reflected in the small deformation monitoring. In practice, the influence of atmospheric errors, topographic errors, space–time baselines, and other decoherence factors caused the actual monitoring ability to decrease relative to the theoretical monitoring, making it difficult to obtain large gradient deformation information from the subsidence basins.

(2) The UAV obtained high-precision and high-resolution point cloud data of mining subsidence areas by periodic aerial surveys on the ground. The DEM was then generated by filtering and a ground point interpolation. Finally, the large gradient subsidence of surfaces was obtained by superimposing and subtracting the two DEMs. However, its edge expression ability was poor and unable to monitor small subsidence deformations.

(3) The combination of the DInSAR and UAV technologies could more accurately express the surface deformation law of high-strength coal mining areas. This not only made use of the high accuracy of UAV data in the center of subsidence areas, but also retained the advantages of the DInSAR differential results in edge monitoring. This made up for the shortcomings of the DInSAR method for the decoherence of large gradient deformations and UAV technologies in small deformation edge monitoring. The accuracy of the results obtained from the proposed method was improved compared with the singular DInSAR or UAV results. Thus, the fusion results were more consistent with the leveling data. This provides new methods and means for mining subsidence monitoring and has a certain reference value for geological disaster assessments as well as preventing geological disasters and the ecological reconstruction of mining areas.

Author Contributions: Conceptualization, X.L. (Xugang Lian); Data curation, Y.Z., X.L. (Xiaoyu Liu) and Y.W.; Formal analysis, X.L. (Xugang Lian) and Y.W.; Funding acquisition, X.L. (Xugang Lian); Investigation, L.G., X.L. (Xiaoyu Liu) and Y.C.; Methodology, Y.Z. and X.L. (Xiaoyu Liu); Supervision, W.Y.; Validation, L.G., Z.D., W.Y. and Y.C.; Visualization, H.H.; Writing—original draft, Y.Z. and Y.W.; Writing—review & editing, X.L. (Xugang Lian), Z.D. and H.H. All authors have read and agreed to the published version of the manuscript.

Conflicts of Interest: The authors declare no conflict of interest.

References

1. Wang, Y.J. Research Progress and Prospect on Ecological Disturbance Monitoring in Mining Area. *Acta Geod. Cartogr. Sin.* **2017**, *46*, 1705–1716.
2. Lopez-Quiroz, P.; Jaramillo, S.H.; Suarez, G.; Sanchez-Zamora, O. Estimation of ground subsidence in the city of Morelia, Mexico using satellite interferometry (insar)s. *Geofís. Int.* **2018**, *57*, 39–58.
3. Antonielli, B.; Sciortino, A.; Scancella, S.; Bozzano, F.; Mazzanti, P. Tracking Deformation Processes at the Legnica Glogow Copper District (Poland) by Satellite InSAR—I: Room and Pillar Mine District. *Land* **2021**, *10*, 653. [CrossRef]
4. Bitelli, G.; Bonsignore, F.; Del Conte, S.; Novali, F.; Pellegrino, I.; Vittuari, L. Integrated use of Advanced InSAR and GPS data for subsidence monitoring. *Eng. Geol. Soc. Territ.* **2015**, *5*, 147–150.

5.   Yang, Z.; Li, Z.W.; Zhu, J.J.; Yi, H.W.; Hu, J.; Feng, G.C. Deriving Dynamic Subsidence of Coal Mining Areas Using InSAR and Logistic Model. *Remote Sens.* **2017**, *9*, 125. [CrossRef]

6.   Zhu, J.; Xing, X.; Hu, J.; Li, Z. Monitoring of ground surface deformation in mining area with insar technique. *Zhongguo Youse Jinshu Xuebao/Chin. J. Nonferrous Met.* **2011**, *21*, 2564–2576.

7.   Novellis, D.N.; Castaldo, R.; Luca, C.D.; Pepe, S.; Zinno, I.; Casu, F.; Lanari, R.; Solaro, G. Source modelling of the 2015 Wolf volcano (Galapagos) eruption inferred from Sentinel 1-A DInSAR deformation maps and pre-eruptive ENVISAT time series. *J. Volcanol. Geotherm. Res.* **2017**, *344*, 246–256. [CrossRef]

8.   Yang, Z.F.; Li, Z.W.; Zhu, J.J.; Yi, H.W.; Peng, G.C.; Hu, J.; Wu, L.X.; Preusse, A.; Wang, Y.J.; Papst, M. Locating and defining underground goaf caused by coal mining from space-borne sar interferometry. *ISPRS J. Photogramm. Remote Sens.* **2018**, *135*, 112–126. [CrossRef]

9.   Modeste, G.; Doubre, C.; Masson, F. Time evolution of mining-related residual subsidence monitored over a 24-year period using InSAR in southern Alsace, France. *Int. J. Appl. Earth Obs. Geoinf.* **2021**, *102*, 102392. [CrossRef]

10. Gabriel, A.K.; Goldstein, R.M.; Zebker, H.A. Mapping small elevation changes over large areas: Differential radar interferometry. *J. Geophys. Res. Solid Earth* **1989**, *94*, 9183–9191. [CrossRef]

11. Carnec, C.; Massonnet, D.; King, C. Two examples of the use of sar interferometry on displacement fields of small spatial extent. *Geophys. Res. Lett.* **1996**, *24*, 3579–3582. [CrossRef]

12. Alex, H.; Ge, L.L.; Yan, Y.G.; Li, X.J.; Chang, H.; Zhang, K.; Rizos, C. Mapping accumulated mine subsidence using small stack of sar differential interferograms in the southern coalfield of new south wales, Australia. *Eng. Geol.* **2010**, *115*, 1–15.

13. Yastika, P.E.; Shimizu, N.; Abidin, H.Z. Monitoring of long-term land subsidence from 2003 to 2017 in coastal area of semarang, indonesia by sbas dinsar analyses using envisat-asar, alos-palsar, and sentinel-1a sar data. *Adv. Space Res.* **2019**, *63*, 1719–1736. [CrossRef]

14. Carnec, C.; Delacourt, C. Three years of mining subsidence monitored by sar interferometry, near Gardanne, France. *J. Appl. Geophys.* **2000**, *43*, 43–54. [CrossRef]

15. Simmons, B.S.; Wempen, J.M. Quantifying relationships between subsidence and longwall face advance using dinsar. *Int. J. Min. Sci. Technol.* **2020**, *31*, 91–94. [CrossRef]

16. Ge, L.L.; Rizos, C.; Han, S.W.; Zebker, H.A. Mining Subsidence monitoring using the combined InSAR and GPS approach. In Proceedings of the 10th FIG International Symposium on Deformation Measurements, Orange, CA, USA, 19–22 March 2001.

17. Lian, X.G.; Wu, Y.R.; Ge, L.L.; Du, Z.Y.; Liu, X.Y. DInSAR Monitoring of Surface Subsidence by Fusing Sentinel-1A and -1B Data to Improve Time Resolution in a Mining Area. *Can. J. Remote Sens.* **2021**, *27*, 596–606. [CrossRef]

18. Gasperini, D.; Allemand, P.; Delacourt, C.; Grandjean, P. Potential and limitation of UAV for monitoring subsidence in municipal landfills. *Int. J. Environ. Technol. Manag.* **2014**, *17*, 1–13. [CrossRef]

19. Liu, J.; Wang, H.; Wang, Q.; Liu, X. Application of uav remote sensing technology in open-pit slop mapping. *Infrared Laser Eng.* **2016**, *45*, 118–121.

20. Stupar, D.; Roer, J.; Vuli, M. Investigation of unmanned aerial vehicles-based photogrammetry for large mine subsidence monitoring. *Minerals* **2020**, *10*, 196. [CrossRef]

21. Chen, J.P.; Li, K.; Chang, K.J.; Giulia, S.; Paolo, T. Open-pit mining geomorphic feature characterisation. *Int. J. Appl. Earth Obs. Geoinf.* **2015**, *42*, 76–86. [CrossRef]

22. Ge, L.L.; Li, X.J.; Ng, A.H. UAV for mining applications: A case study at an open-cut mine and a longwall mine in New South Wales, Australia. In Proceedings of the 2016 IEEE International Geoscience and Remote Sensing Symposium (IGARSS), Beijing, China, 10–15 July 2016; pp. 5422–5425.

23. Ćwiąkała, P.; Gruszczyński, W.; Stoch, T.; Puniach, E.; Mrocheń, D.; Matwij, W.; Matwij, K.; Nędzka, M.; Sopata, P.; Wójcik, A. Uav applications for determination of land deformations caused by underground mining. *Remote Sens.* **2020**, *12*, 1733.

24. Lian, X.G.; Liu, X.Y.; Ge, L.L.; Hu, H.F.; Wu, Y.R. Time-series unmanned aerial vehicle photogrammetry monitoring method without ground control points to measure mining subsidence. *J. Appl. Remote Sens.* **2021**, *15*, 024505. [CrossRef]

25. Zebker, H.A.; Villasenor, J. Decorrelation in Interferometric Radar Echoes. *IEEE Trans. Geosci. Remote Sens.* **1992**, *30*, 950–959. [CrossRef]

26. Yao, S.Y.; Yang, K.M.; Dong, X.L.; Shi, X.Y.; Wang, J. Large-gradient deformation monitoring and parameter inversion in a mining area using a method combining a dynamic prediction model and InSAR. *Remote Sens. Lett.* **2021**, *12*, 838–847. [CrossRef]

27. Jiang, C.; Wang, L.; Yu, X.X.; Wei, T.; Chi, S.S.; Guo, Q.B. Prediction of 3D deformation due to large gradient mining subsidence based on InSAR and constraints of IDPIM model. *Int. J. Remote Sens.* **2021**, *42*, 208–239. [CrossRef]

28. Ding, L.J.; Tao, Q.X.; Gao, T.F.; LI, X.; Sun, C.Y. Application of sbas insar in monitoring mining land subsidence. *China Sci.* **2019**, *14*, 320–325.

29. Zhu, J.J.; Yang, Z.F.; Li, Z.W. Recent progress in retrieving and predicting mining-induced 3D displacements using InSAR. *Acta Geod. Cartogr. Sin.* **2019**, *48*, 135–144. [CrossRef]

30. Zhang, S.; Lv, Y.H.; Yang, H.Y.; Han, Y.; Peng, J.Y.; Lan, J.W.; Zhan, L.T.; Chen, Y.M.; Bate, B. Monitoring and Quantitative Human Risk Assessment of Municipal Solid Waste Landfill Using Integrated Satellite–UAV–Ground Survey Approach. *Remote Sens.* **2021**, *13*, 4496. [CrossRef]

31.　Deffontaines, B.; Chang, K.; Champenois, J.; Fruneau, B.; Pathier, E.; Hu, J.; Lu, S.; Liu, Y. Active interseismic shallow deformation of the Pingting terraces (Longitudinal Valley–Eastern Taiwan) from UAV high-resolution topographic data combined with InSAR time series. *Geomat. Nat. Hazards Risk* **2016**, *8*, 120–136.

32.　Meng, Q.K.; Li, W.L.; Raspini, F.; Xu, Q.; Peng, Y.; Ju, Y.Z.; Zheng, Y.Z.; Casagli, N. Time-series analysis of the evolution of large-scale loess landslides using InSAR and UAV photogrammetry techniques: A case study in Hongheyan, Gansu Province, Northwest China. *Landslides* **2021**, *18*, 251–265. [CrossRef]

33.　Wang, L.; Jiang, C.; Wei, T.; Li, N.; Chi, S.S.; Zha, J.F.; Fang, S.Y. Robust estimation of angular parameters of the surface moving basin boundary induced by coal mining: A case of huainan mining area. *KSCE J. Civ. Eng.* **2020**, *24*, 266–277. [CrossRef]

34.　Baran, I.; Stewart, M.; Claessens, S. A new functional model for determining minimum and maximum detectable deformation gradient resolved by satellite radar interferometry. *IEEE Trans. Geosci. Remote Sens.* **2005**, *4*, 675–682. [CrossRef]